Applied Thermal Engineering 230 (2023) 120758

Contents lists available at ScienceDirect

Applied Thermal Engineering

journal homepage: www.elsevier.com/locate/apthermeng

Research Paper

Thermal boundary layer depletion in minichannels by electrohydrodynamic conduction pumping

R. Deepak Selvakumar [a,b], Hyoungsoon Lee [b,c,*]

[a] Department of Nuclear Engineering, Khalifa University of Science and Technology, Abu Dhabi, UAE
[b] School of Mechanical Engineering, Chung-Ang University, Seoul 06974, South Korea
[c] Department of Intelligent Energy and Industry, Chung-Ang University, Seoul 06974, South Korea

ARTICLE INFO

Keywords:
Thermal management
Flexible electronics
Minichannel
EHD conduction pumping
Electrohydrodynamics

ABSTRACT

The article presents a numerical analysis of two-dimensional laminar flow and heat transfer in a minichannel with flat plate electrode pairs periodically flushed to the bottom wall. The two-way coupled governing equations of flow, heat transfer, electric potential and charge conservation are solved using the opensource finite-volume framework of OpenFOAM. Two cases of the minichannel at completely horizontal (case A) and 90° bent (case B) configurations are considered. The inlet laminar flow with Reynolds number varying from 10 to 1000 has been taken into account. The applied electric potential is varied in three steps 0, 0.5 and 1 kV. Electrohydrodynamic (EHD) conduction pumping due to the residual conductivity of the working fluid and the electric-field enhanced dissociation of free charges generate vortices in the proximity of electrodes. The flow and thermal performance of the minichannel in the presence of EHD conduction induced vortices are quantified in terms of pressure drop, Nusselt number and a performance factor (which is a combined function of pressure drop and Nusselt number). The vortices generated by EHD conduction pumping phenomenon deplete the thermal boundary layer, aid mixing and enhance the heat transfer. The mean and local Nusselt numbers are notably increased with only a minimal raise in pressure drop. In both the configurations of the minichannel, the performance factor is greater than 1 for the entire parameter space considered in this study. However, the thermal boundary layer depletion and heat transfer enhancement is prominent at low Reynolds number flows. The maximum drop in performance factor from case A to case B is only 18.5%. Results of this study indicate that EHD conduction pumping is a potential technique to enhance heat transfer in minichannels with minimum additional power consumption.

1. Introduction

Performance of modern-day high-tech devices depend on efficient cooling of their components like power transformers, processors and electronic chip boards, etc. The recent trend of miniaturization, thinness, and lightness in electronic devices result in high-density heat fluxes. High heat flux generation over a small surface area leads to overheating, poor performance, and malfunctioning of electronic devices. For these reasons, it is important to develop a compact, effective and efficient thermal management technique for ensuring sustainable cooling of mini/micro-scale electronic devices [1]. Commonly used heat transfer technologies such as conventional heat sinks, pin fin arrays, fan-assisted heat sinks cooled by air have limited heat transfer capability and are unsuitable for incorporation into mini/micro-scale electronic devices [2]. Minichannels are an attractive option for the thermal management of small-sized power electronic devices. The large surface-area-to-volume ratio of minichannels helps to effectively dissipate heat from localized hotspots, and their small size makes it easier to incorporate them into compact electronic devices [3]. However, owing to small dimensions and low Reynolds number flows in minichannels, the flows in them are generally laminar. Thus, the resultant mixing and heat transfer in a smooth and straight minichannel is limited by the viscous and thermal boundary layers [4,5]. Furthermore, the pressure drop incurred to achieve high flow rates to dissipate high density heat fluxes is very high in mini/microchannels. Thus, high heat transfer coefficients in mini/microchannel flows at large flow rates are always accompanied by exponential increase in the pumping power requirement [5].

Heat transfer enhancement in minichannels has been studied extensively in the last two decades [6,7]. Researchers have proposed several passive and active techniques to enhance heat transfer in

* Corresponding author.
E-mail address: leeh@cau.ac.kr (H. Lee).

https://doi.org/10.1016/j.applthermaleng.2023.120758
Received 31 October 2022; Received in revised form 17 April 2023; Accepted 8 May 2023
Available online 12 May 2023
1359-4311/

minichannels. Among them, passive techniques include surface roughness, flow disruption, channel curvature, re-entrant cavities, and fluid additives. Active methods include the introduction of a secondary flow, vibration, flow pulsation, and application of magnetic and electrostatic fields. Active methods with low energy consumption represent attractive choices for enhancing heat transfer in conventional and minichannels. In this context, electrohydrodynamic (EHD) flow-based techniques have been used by several researchers to enhance heat transfer in channel flows [8]. EHD-based techniques offer several advantages such as simple design, low power consumption, quick response, lack of moving parts, lack of noise and vibration, durability, and easy incorporation into electronic devices. In EHD systems, the Coulomb force induced by an electric field result in motion of the dielectric fluid. EHD-induced fluid motion can generally be classified into three types as follows: (i) EHD induction pumping, (ii) ion-drag or ion-injection pumping, and (iii) EHD conduction pumping [9]. EHD induction pumping is based on gradient/discontinuity in the electrical conductivity of the working dielectric fluid. A temperature gradient is imposed on the dielectric medium, which results in a gradient of electric conductivity. The gradient/discontinuity in electric conductivity leads to localized accumulation of free charges. When a wave electric field is applied, the accumulated charges are attracted toward the energized electrodes. This results in bulk motion of the dielectric medium [10]. However, EHD induction pumping is less popular among researchers because it requires a working dielectric fluid whose electric conductivity strongly varies with respect to temperature. Moreover, EHD induction pumping requires a complex electrode system to apply a moving time-dependent wave electric field. Ion- drag or ion-injection pumping is based on the charge injection that takes place at the high-voltage electrodes. When a strong electric voltage is applied on an electrode, electrochemical reactions occur at the dielectric medium–electrode interface. Because of these reactions, free charges are injected from the electrode surface into the dielectric medium. These charges move toward the oppositely charged electrode while transferring momentum to the bulk fluid [11]. Ion-drag pumping generates bulk fluid motion in macroscopic scales with significant velocity and flow rates. Hence, ion-drag pumping is the most extensively studied EHD flow technique. The majority of the studies on EHD-based heat transfer enhancement pertain to ion-drag pumping [9]. However, in ion-drag pumping, an extremely high electric potential is required to induce charge injection, which is potentially unsafe for consumer electronic cooling applications. Furthermore, continuous charge injection from the electrode, degrades the electrodes and the working electrolyte. Thus, EHD flow techniques based on charge injection are less reliable, inconsistent, and unsuitable for sustainable cooling over extended durations.

EHD conduction pumping is based on charge generation through ion dissociation. In a dielectric medium, a small number of free charges exist owing to impurities and exposure to the ambient environment. These free charges undergo dissociation and recombination due to an applied electric field. In general, dissociation and recombination rates are equal. There exists a threshold voltage, above which the dissociation rate exceeds the recombination rate. This phenomenon is termed “field-enhanced dissociation” or “Onsager–Wien effect” [12,13]. Because of the Onsager–Wien effect, more free charges are generated in the proximity of the electrodes. Thus, a layer of free charges termed as “hetero-charge layer” develops over the electrodes. Owing to the unequal rates of dissociation and recombination of free charges/ions within the hetero-charge layer, the residual charges move toward the oppositely charged electrode while inducing a motion in the surrounding fluid. Ideally, the net fluid flow due to the movement of opposite charges is zero. However, use of electrodes with different surface areas can result in an imbalance in the movement of charges, and hence, a net fluid motion can be generated. The threshold voltage required for the Onsager–Wien effect is considerably lower than that required for ion-drag pumping, and hence, does not cause any electrode degradation. Furthermore, unlike induction pumping, EHD conduction pumping does not require any special dielectric liquid or electrode design. Thus, EHD conduction pumping overcomes the drawbacks of charge injection pumping and charge induction based EHD pumping. However, the flow generated by EHD conduction pumping is extremely weak (mini/microscale). For instance, the net flow rate and velocities generated by the Onsager-Wien effect are two orders of magnitude smaller than those generated by ion-drag pumping [9]. Thus, the EHD conduction pumping flow due to Onsager–Wien effect becomes more suitable for mini or micro-scale flow and heat transfer applications.

EHD conduction pumping is not popular among researchers in comparison with charge injection based EHD pumping. The analytical model for the EHD conduction pumping flow due to residual conductivity and Onsager-Wien effect was first reported by Atten and Seyed-Yagoobi [14]. Based on their pioneering work, further developments in the analytical and numerical modelling were carried out by other researchers [15-18]. Experimental studies on EHD conduction pumping have been performed using various electrode configurations, and their results have been compared with those of the analytical models [18-20]. In view of the microscale motion generated by the Onsager–Wien effect, several researchers have attempted to develop an EHD-conduction-based micropump for microfluidic applications. Pearson and Yagoobi [21] developed an EHD conduction pump that produced notable flow rates at the meso and microscales, even under a small applied voltage of 0.75 kV. Kano and Nishina [22] experimentally studied the effect of electrode arrangement on the efficiency of EHD conduction pumping. A maximum flow rate of 2.5 mL/min was reported at an applied voltage of 1 kV with asymmetric electrode arrangement. Patel and Seyed-Yagoobi [23] experimentally evaluated the performance of a pump based on EHD conduction over a long operating period. The EHD conduction pump’s ability to operate continuously for 105 h without any performance deterioration was demonstrated. Du et al. [24] numerically studied the interaction of EHD conduction pumping with an external cross flow. The influence of direction of external flow on EHD conduction pumping was evaluated. In the above-referenced studies, the ability of EHD conduction to pump fluid in microfluidic applications was evaluated. Pearson and Yagoobi [25,26] experimentally studied single/two-phase flows driven by EHD conduction pumping in a microchannel. The flow rate produced by the EHD conduction pumping alone was insufficient to effectively dissipate the applied heat flux. However, when aided by an external flow, the heat transfer due to the EHD fluid motion improved notably. Pearson and Seyyed-Yagoobi [27] experimentally showcased the performance of EHD conduction pumping in a two-phase heat pipe. EHD conduction pumping was able to pump a thin dielectric liquid film efficiently along a vertical surface. Notable increase in heat transfer with minimum additional electric power consumption was achieved. Patel et al. [28] experimentally tested the ability of EHD-conduction-pumping-driven flow-boiling in a nanofiber-enhanced surface. The boiling heat transfer coefficient increased several folds upon the use of a combination of EHD conduction pumping and nano-textured surface. Selvakumar et al. [29] numerically demonstrated the ability of EHD conduction pumping to dissipate localized high-density heat flux in electronic cooling applications. The flow vortices induced by the Onsager–Wien effect led to thinning of the thermal boundary layer and enhanced heat transfer by up to 31.2%.

All of these referenced works attemp to induce or enhance heat transfer by introducing a flow by using EHD conduction pumping phenomenon. Although several promising results were reported, EHD conduction pumping alone could not induce a flow rate that is adequate for dissipating high-density heat fluxes. Furthermore, EHD conduction pumping based on the electric field enhanced dissociation has been explored less sparsely compared to ion-drag pumping. In this context, we propose a novel idea to use EHD conduction pumping to deplete the laminar viscous and thermal boundary layers in a flexible minichannel. The proposed method employs vortices generated by EHD conduction pumping mechanism to disrupt the boundary layers and enhance mixing. Thus, expected to incur minimal raise in pressure drop and minimal additional electrical power consumption. A numerical demonstration and analysis of small vortices induced by EHD conduction phenomenon and the resultant thermal boundary layer depletion, mixing and heat transfer enhancement in a flexible minichannel are presented. It is to be noted that the flexible minichannels incorporated in flexible electronic devices are flexible enough to be straight or bent positions but, they stay rigid at any given position. Thus, two cases A and B of a minichannel rigidly held straight and 90° bent configurations, respectively are considered in this study. The mechanism of depletion of boundary layer by EHD vortices is highlighted. The flow and heat transfer performances of the minichannel are studied in a wide range of inlet flow Reynolds numbers and applied voltages.

2. Problem formulation

2.1. Channel geometry and arrangement of electrodes

A 2-D minichannel with length $L = 200mm$ and height $H = 20mm$ is considered. The working fluid is initially at ambient temperature $T_\infty = T_{in} = 293.15K$. The bottom wall of the minichannel is heated with a uniform heat flux $q_w = 10000\mathrm{W/m^2}$. The top wall is considered to be adiabatic. The left boundary is the fluid inlet with uniform inlet velocity U_{in} in the positive x-direction. The right boundary of the domain is the fluid outlet. Bottom wall of the channel has 10 electrode pairs. The electrodes are considered to be very thin (with negligible thickness) and are flushed in the bottom wall of the channel. Each electrode pair consists of a small high voltage electrode of length $3mm$, which is separated by a gap of $d = 3mm$ from the grounded electrode of length $9mm$. Two configurations of the channel are considered. Case A considers the channel to be horizontal ($\gamma = 0^\circ$). Case B considers the channel to be bent $\gamma = 90^\circ$, with the inlet perfectly vertical and the outlet being perfectly horizontal. The top wall and the gaps in the bottom wall are electrically insulated. A schematic representation of the flow configuration is shown in Fig. 1.

2.2. Governing equations

The numerical model for the two-way coupled laminar flow and heat transfer in the presence of secondary EHD conduction pumping flow is developed under the following assumptions [30]:

a) Transient, two-dimensional (2D), laminar and incompressible fluid flow.
b) Constant thermophysical and dielectric properties.
c) Viscous dissipation, Joule heating and radiation are negligible.

In the context of above assumptions, the flow field is governed by the incompressible Navier-Stokes equations, which are expressed as Eqs. (1) and (2):

$$\nabla.\vec{u} = 0 \tag{1}$$

$$\frac{\partial \vec{u}}{\partial t} + \nabla.(\vec{u}\,\vec{u}) = -\nabla p + \rho\vec{g} + \upsilon\nabla^2\vec{u} + \vec{F}_E \tag{2}$$

Here, $\vec{u}$ is the flow field velocity, p is the pressure, and υ is the kinematic viscosity of the working fluid. $\rho\vec{g}$ represents the gravitational body force term. The density ρ is calculated by the Boussinesq approximation as $\rho = [1 - \beta(T - T_{ref})]$. Here, β is the thermal expansion coefficient and $T_{ref} = 293.15K$ is the reference temperature. The additional source term $\vec{F}_E$ is the body force due to electric field. The temperature distribution is given by the energy equation Eq. (3).

$$\frac{\partial T}{\partial t} + \vec{u}.\nabla T = \nabla.(\alpha\nabla T) \tag{3}$$

In Eq. (3), T represents the temperature, and α denotes thermal diffusivity of the working fluid.

The electric field $\vec{E}$ is calculated as the divergence of applied electric potential as $\vec{E} = -\nabla V$. The distribution of electric potential V is given as follows:

$$\nabla.(\varepsilon\nabla V) = -q_c \tag{4}$$

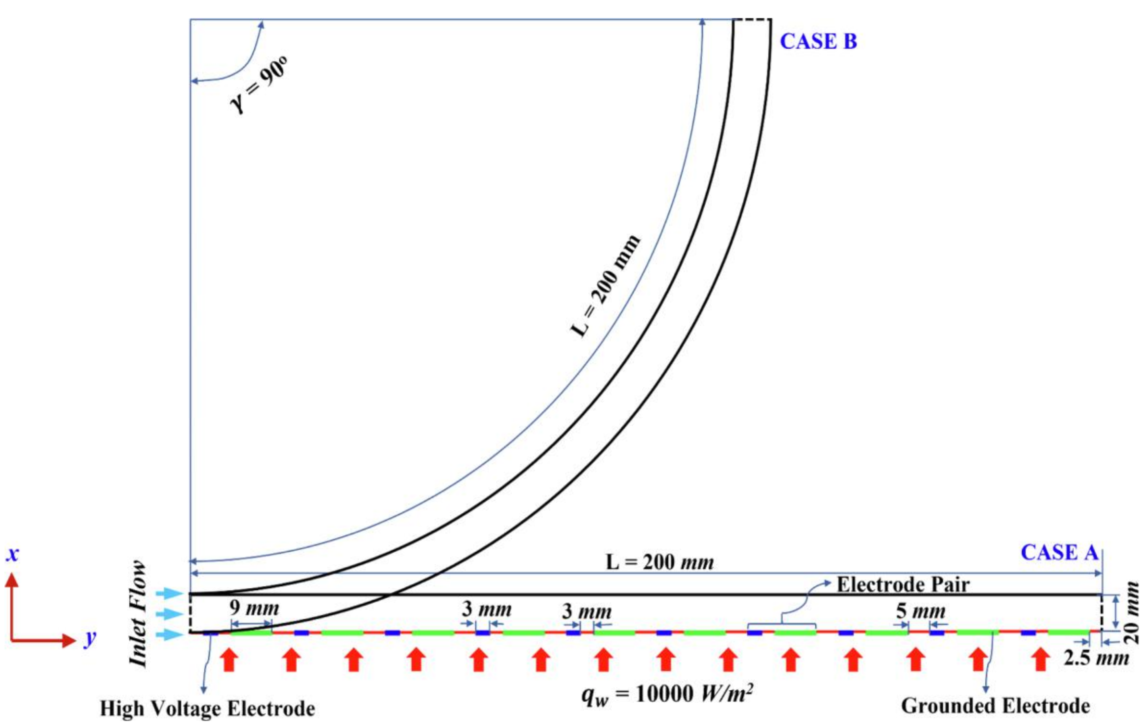

Fig. 1. Schematic representation of the computational domain.

Here, ε represents the dielectric permittivity of the fluid, and $q_c = p - n$ is the space charge density. p and n are the positive and negative charge densities, respectively. The conservation of the positive and negative charges in the presence of an external electric field is expressed as:

$$\frac{\partial p}{\partial t} + \nabla.\left[\vec{u}p + K\vec{E}p - Dp\right] = R_p \tag{5}$$

$$\frac{\partial n}{\partial t} + \nabla.\left[\vec{u}n + K\vec{E}n - Dn\right] = R_n \tag{6}$$

In the above equations, K and D denote the ionic mobility and ionic diffusivity of the fluid, respectively. $R_{p,n}$ represents the reaction term comprising the dissociation and recombination processes, and it is expressed as $R_{p,n} = k_d N - k_r pn$ [14]. Here, k_d is the dissociation rate of neutral species, and $k_r = \frac{2K}{\varepsilon}$ is the recombination rate of positive and negative ions. Under equilibrium conditions, the dissociation rate k_d of neutral species and the recombination rates of positive and negative ions are equal. In other words, the neutral species is dissociated into positive and negative charges, which is followed by complete recombination of the positive and negative ions to form the original neutral species. Thus, under equilibrium conditions, the reaction term can be expressed as $R_{p,n(eq)} = k_{d(eq)}N - k_r p_{eq} n_{eq} = 0$. Here, the subscript "$eq$" represents the equilibrium conditions. The charge densities of positive and negative ions under the equilibrium conditions are expressed as follows:

$$p_{eq} = n_{eq} = \frac{\sigma}{2K} = N \tag{7}$$

where σ is the electrical conductivity. However, beyond a certain threshold voltage, the applied electric field enhances the dissociation rate due to the Onsager–Wien effect. Thus, k_d exceeds $k_{d(eq)}$. According to the Onsager model, $k_d = k_{d(eq)}F(b)$ [31]. Here, $F(b)$ is the Onsager function for field-enhanced dissociation. Moreover, $b^2 = (l_B/l_0)^2 = 4\gamma\vec{E}$, $\gamma = e^3/16\pi\varepsilon k_B^2 T^2$, and $F(b) = I_1(2b)/b$. $l_B = e^2/4\pi\varepsilon k_B T$ is the Bjerrum distance [32], k_B is Boltzmann's constant, and e denotes the basic electric charge. The function I_1 represents a modified Bessel function of first kind and order one [11,31,32]. The function I_1 can be expanded as an ascending series as $I_1(x) = \sum_{k=0}^{\infty}\frac{(x/2)^{1+2k}}{k!(k+1)!}$. Thus, the reaction term $R_{p,n} = k_{d(eq)}NF(b) - k_r pn$.

The body force term $\vec{F}_E$ due to electric field in Eq. (2) can be expressed as follows [11,33]:

$$\vec{F}_E = q_c\vec{E} - \frac{1}{2}\vec{E}\nabla\varepsilon + \frac{1}{2}\left[\vec{E}^2\left(\frac{\partial\varepsilon}{\partial\rho}\right)\rho\right] \tag{8}$$

The right-hand side of Eq. (9) consists of three terms, namely (i) Coulomb force, (ii) dielectrophoretic force, and (iii) electrostriction force. In an incompressible, single-phase fluid with poor temperature-dependent dielectric permittivity, the dielectrophoretic force and electrostriction force terms become zero. Thus, present study considers only the Coulomb force $q_c\vec{E}$.

2.3. Boundary conditions

No slip and no penetration boundary conditions are applied over the horizontal walls of the channel. At the channel inlet, a uniform inlet velocity U_{in} in the positive x-direction is considered. Pressure outlet boundary condition is applied at the right vertical boundary (channel outlet) of the channel. The bottom wall including the electrode surfaces is exposed to a constant, uniform heat flux of $q_w = 10000 W/m^2$. The entire top wall is thermally insulated. The inlet temperature of the working fluid is $T_{in} = 293.15K$. The short electrodes flushed along the bottom wall of the channel are connected to a high electric potential V. The longer electrodes are grounded ($V = 0$). Electrode gaps in the bottom wall and the complete top wall are electrically insulated. The Dirichlet boundary condition for positive ions ($p = 0$) and the Neumann boundary condition $(\partial n/\partial y) = 0$ for negative ions are applied to the high-voltage electrodes. Likewise, the Dirichlet boundary condition for negative ions ($n = 0$) and the Neumann boundary condition for positive ions ($(\partial p/\partial y) = 0$) are applied to the grounded electrodes. The boundary conditions are summarized in Table 1.

2.4. Material properties

In the present study, the working fluid is deionized (DI) water. The properties of DI water are summarized in Table 2. All properties are constant with respect to temperature. The ionic mobility of DI water is calculated using Walden's rule [34] as $K = 1.5 \times 10^{-11}/\mu$. Likewise, the ionic diffusivity of DI water is calculated using Einstein's relation [13] as $D = K k_B T_{ref}/e$. Here, T_{ref} is the ambient temperature $T_\infty = 293.15K$.

2.5. Governing and evaluation parameters

The governing and evaluation parameters of interest used in this study are presented in this section. In the problem considered herein, fluid motion is driven by two factors, namely (i) the base flow set by the inlet velocity and (ii) the flow vortices induced by EHD conduction pumping phenomenon due to the applied electric potential. The base flow in the minichannel is characterized by the flow Reynolds number Re, which is defined as

$$Re = \frac{\rho U_{in} H}{\mu} \tag{9}$$

Here, ρ is the fluid density, U_{in} is the uniform inlet velocity in the positive x–direction, and H is the channel height. The inlet flow Reynolds number considered herein is $10 \le Re \le 1000$. The fluid motion induced by the EHD conduction pumping is characterized by the magnitude of applied electric potential. The electric potential is varied in three levels 0, 0.5 and 1 kV. The average friction factor f is calculated based on the pressure drop Δp across the total channel length L as follows [35]:

$$f = \frac{2\Delta p D_H}{\rho_f L U_{av}^2} \tag{10}$$

In Eq. (10), U_{av} is the mean fluid velocity in the flow domain. The expressions for local heat transfer coefficient and the local Nusselt number as follows:

$$h(x) = \frac{q_w}{T - T_{in}} \text{ and } Nu(x) = \frac{h(x)H}{k} \tag{11}$$

In the expression for local Nusselt number, k is the fluid thermal conductivity. The average Nusselt number is obtained as $Nu_M = \frac{1}{L}\int_{x=0}^{L} Nu(x).dx$. The performance factor, a function of both heat transfer

Table 1
Summary of boundary conditions.

Location	Condition
High-voltage electrodes	$u_x = u_y = u_z = 0; q_w = 10000 Wm^{-2}; V > 0; p = 0; \frac{\partial n}{\partial y} = 0$
Grounded electrodes	$u_x = u_y = u_z = 0; q_w = 10000 Wm^{-2}; V = 0; n = 0; \frac{\partial p}{\partial y} = 0$
Top wall ($y = 20mm$)	$u_x = u_y = u_z = 0; \frac{\partial T}{\partial y} = 0; \frac{\partial V}{\partial y} = 0; \frac{\partial n}{\partial y} = 0; \frac{\partial p}{\partial y} = 0$
Bottom wall ($y = 0mm$)	$u_x = u_y = u_z = 0; q_w = 10000 Wm^{-2}; \frac{\partial V}{\partial y} = 0; \frac{\partial p}{\partial y} = 0; \frac{\partial n}{\partial y} = 0$
Inlet ($x = 0$)	$u_x = U_{in}; u_y = u_z = 0; T_{in} = 293.15K; \frac{\partial V}{\partial x} = 0; \frac{\partial p}{\partial x} = 0; \frac{\partial n}{\partial x} = 0$
Outlet ($x = 200mm$)	$\frac{\partial u}{\partial x} = 0; \frac{\partial T}{\partial x} = 0; \frac{\partial V}{\partial x} = 0; \frac{\partial p}{\partial x} = 0; \frac{\partial n}{\partial x} = 0$

Table 2
Properties of the working fluid (deionized (DI) water).

Property	Value
Density $[kg/m^3]$	998.2
Thermal conductivity $[W/mK]$	0.59801
Viscosity $[kg/ms]$	0.001001
Specific heat $[J/kgK]$	4185
Thermal expansion coefficient $[1/K]$	210×10^{-6}
Dielectric permittivity $[F/m]$	7.08×10^{-10}
Ionic mobility $[m^2/Vs]$	1.50×10^{-08}
Ionic diffusivity $[m^2/s]$	3.79×10^{-10}
Electric conductivity $[S/m]$	5.50×10^{-06}

enhancement and pressure drop penalty, is defined as follows [36]:

$$PF = \frac{Nu_{M(Re_{EL}>0)}/Nu_{M(Re_{EL}=0)}}{\left(\Delta P_{Re_{EL}>0}/\Delta P_{Re_{EL}=0}\right)^{1/3}} \tag{12}$$

3. Numerical methodology and code validation

3.1. Numerical methodology

The mass, momentum, energy, electric potential and charge conservation equations are solved using the open-source software package OpenFOAM. The equations for the electric potential and charge con-

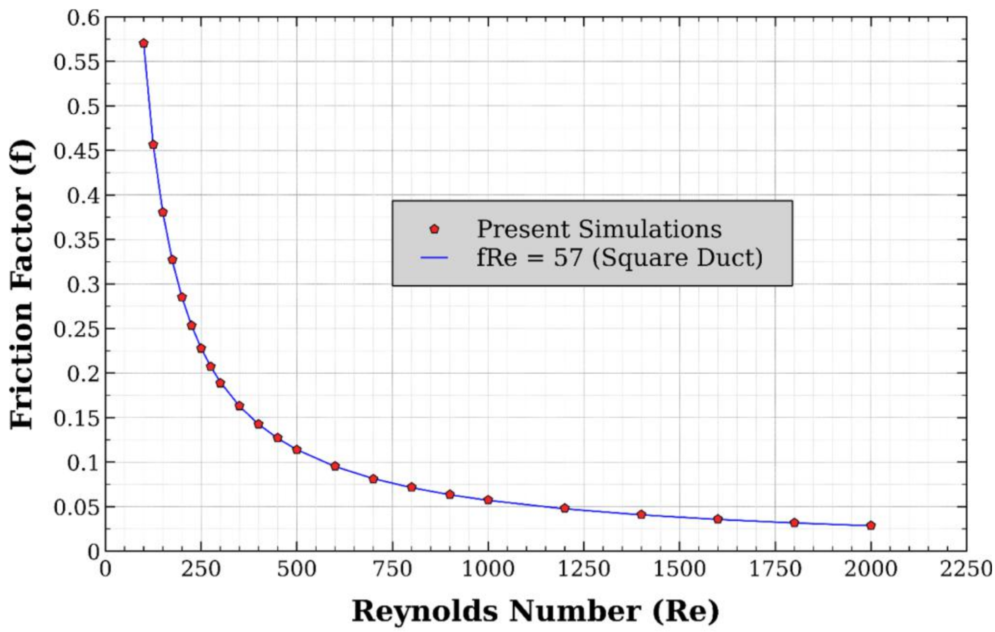

(a)

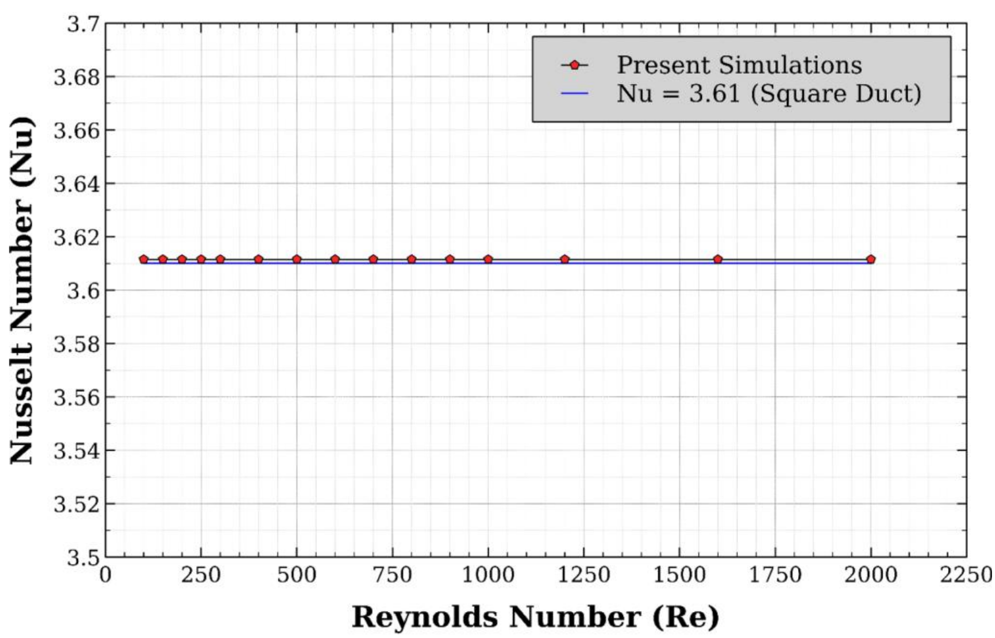

(b)

Fig. 2. Comparison of (a) Friction factor and (b) Nusselt number with correlations for a fully developed laminar flow in a square duct [39].

servation are incorporated into the existing finite-volume framework available in OpenFOAM. The governing equations are discretized based on standard finite-volume procedures available in OpenFOAM. The linear scheme is used to discretize the Laplacian terms, and cubic scheme is used to discretize the gradient terms. Total variation diminishing (TVD) Van Leer scheme [37] is used to discretize the convection derivatives. The time derivatives are discretized using an implicit Euler backward method. A PIMPLE-algorithm-based iterative procedure is applied to solve the discretized set of equations [38]. The sparse matrices obtained from the discretization procedure are solved with an absolute tolerance of 1×10^{-8}.

3.2. Verification of fully developed laminar flow and heat transfer in a square channel

The numerical solver used to solve the fluid flow and heat transfer problem coupled with a secondary EHD conduction pumping flow is validated by comparing with two benchmark cases.

First, the present numerical model is tested with respect to a fully developed laminar flow and heat transfer in a smooth square channel. Fully developed laminar flow in a smooth square channel heated by a uniform heat flux is considered. The results obtained by the present numerical model shows good agreement with the exact solution values of friction factor and Nusselt number [39], as seen in Fig. 2 (a - b).

3.3. Verification of EHD conduction pumping flow in a channel

The numerical model adopted in the present study to simulate EHD conduction pumping induced fluid flow used in this study is validated with reference to experimental measurements and finite-element-method-(FEM)-based numerical results reported by Fernandes et al. [40]. The computational domain is setup to mimic the experimental conditions used in ref [40]. A parallel plate electrode configuration with a cylindrical wire electrode at the center of the domain are considered. The no-slip boundary condition is applied over all electrode surfaces. The periodic boundary condition for all variables is applied at the lateral boundaries. The wire electrode is grounded, and the high-voltage power supply is connected to the plate electrodes. A detailed description of the boundary conditions is presented in [40]. A schematic representation of the flow problem is presented in inset image of Fig. 3a. The flow structure and direction obtained in the present simulations (see inset image of Fig. 3b) are consistent with those reported by Fernandes et al. [40]. Fig. 3 (a - c) presents a comparison of the present numerical results with the literature data for y-velocity profiles along an horizontal line $y = 3.75mm$ at applied electric potentials 0.5, 1, and 1.5 kV. The numerical results obtained herein closely match the experimental and FEM results obtained by Fernandes et al. [40]. Thus, the numerical model of EHD conduction pumping flow based on the Onsager–Wien effect used herein is validated.

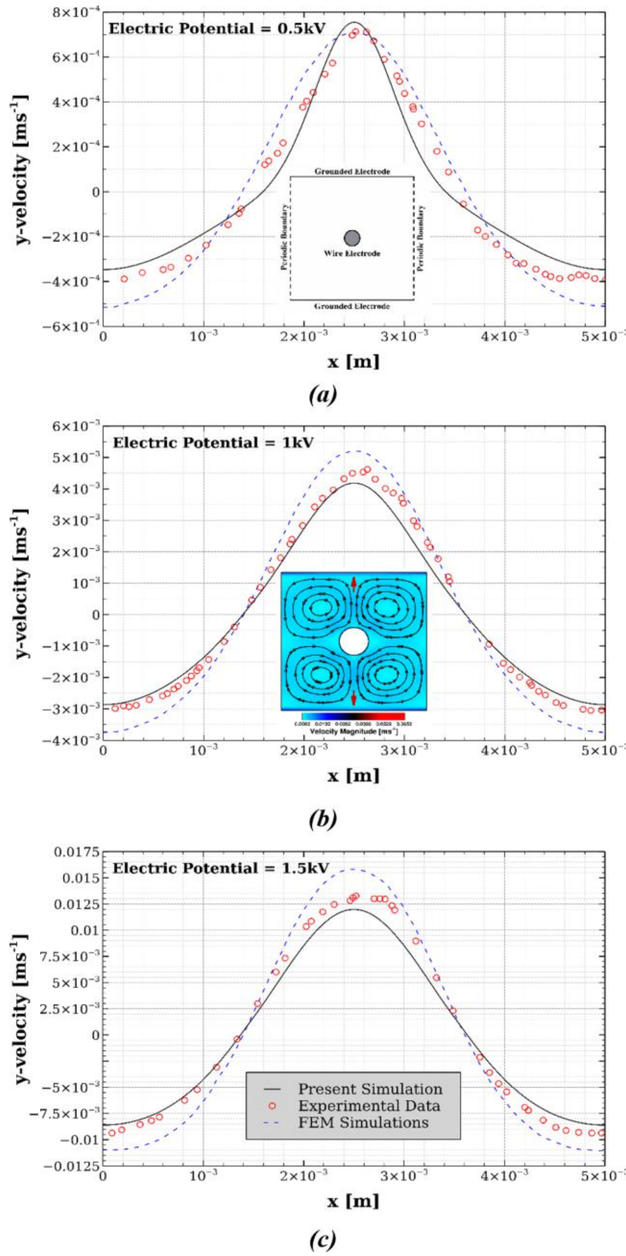

Fig. 3. Comparison of y–velocity profile along $y = 0.35$ mm obtained by present simulations with experimental and numerical results of Fernandes et al. [40]. Flow configuration and the flow structure are presented as inset images.

4. Results and discussion

A numerical study of flow and heat transfer in a flexible minichannel in the presence of EHD conduction pumping flow as an active heat transfer enhancement technique is conducted. In configuration A, the channel is horizontal and in case B, the channel is bent smoothly with an included angle of $\gamma = 90^{\circ}$. In both the configurations, the flow and heat transfer characteristics are studied at $10 \leq Re \leq 1000$ and applied voltages 0, 0.5 and 1 kV. A structured, non-uniform grid with finer cells near the bottom wall chosen based on a grid sensitivity study is used in the simulations presented in this work. The results of the grid sensitivity study are reported in Table 3. Three grids A (660 × 67), B (1320 × 134), and C (2640 × 268) are considered in the grid independence study. The time averaged mean velocity and Nusselt number at $Re = 10$ and 1000 and at $V = 0$ and 1 kV calculated using the three grids for cases A and B are compared. It is seen that the results obtained from grids B and C exhibit less deviation (<1 %) from each other. Thus, grid B is selected for all the simulations presented in this study. Adaptive time stepping method based transient simulations are performed in this study. The criteria for adaptive time stepping are maximum Courant number = 0.5 and maximum time step size is $1 \times 10^{-4}s$. Thus, in all of the simulations, the time step size varied in the range of 1×10^{-5} to $1 \times 10^{-4}s$ and all the simulations were performed up to a physical time equal to 10 s.

4.1. Flow and vortex structure induced by EHD conduction pumping

In an attempt to understand the mechanism of thermal boundary layer depletion by EHD conduction pumping in a minichannel, the first important step is to understand the morphology of the flow vortices induced purely by the EHD conduction pumping. To this end, flow configurations of case A and B without any external flow ($Re = 0$) and heat flux ($q_w = 0$), but with an applied electric potential of $1kV$ are

Table 3
Results of the grid independence study.

Applied Voltage kV	Grid	Mean Nusselt number	% Difference	Mean Velocity m/s	% Difference
CASE A -*Re* $= 10$					
0	A	11.389	–	0.0117	–
	B	11.839	3.81	0.0125	6.40
	C	11.841	0.01	0.0125	0.00
1	A	104.159	–	0.0116	
	B	107.884	3.45	0.0125	7.2
	C	107.884	0.00	0.0126	0.79
CASE A - *Re* $= 10$ **00**					
0	A	73.521	–	1.2501	–
	B	74.722	1.61	1.2535	0.27
	C	74.721	0.01	1.2536	0.00
1	A	90.094	–	1.2494	–
	B	91.227	1.24	1.2535	0.33
	C	91.277	0.00	1.2535	0.00
	CASE B -*Re* $= 10$				
0	A	14.2111	–	0.0095	–
	B	14.3532	0.99	0.0113	15.93
	C	14.3552	0.00	0.0115	1.74
1	A	100.184	–	0.0097	–
	B	101.739	1.53	0.0112	13.39
	C	101.742	0.00	0.0112	0.00
CASE B - *Re* $= 10$ **00**					
0	A	76.603	–	1.1287	–
	B	78.698	2.66	1.1330	0.38
	C	78.692	0.00	1.1330	0.00
1	A	89.993	–	1.1275	–
	B	91.553	1.70	1.1326	0.45
	C	91.550	0.02	1.1327	0.00

considered. Thus, the flow field in the minichannel is induced purely by the EHD conduction pumping. The electric potential and vorticity contours along with velocity vectors in the minichannel for the horizontal configuration (case A), at $t = 10s$ are presented in Fig. 4 (a – b). It is to be noted that all the contours and local values presented in this study are instantaneous values taken at $t = 10s$. Alternate high and low electric potential regions are observed in the proximity of corresponding high voltage and grounded electrodes. Vortices with strong vorticity magnitude are noticed to emanate near the electrodes flushed in the bottom wall of the channel. The vorticity distribution is strong near the electrodes and gets weakened in the vertical direction away from the electrodes. The vortices originate from the smaller high voltage electrodes and rotate towards the wider grounded electrodes. This observation matches with the inference of [41]. Similar observations are also seen in the electric potential and vorticity distributions for case B presented in Fig. 4 (c – d). Application of EHD conduction pumping generates vortices close to the electrodes in the bottom wall. These vortices produced by the EHD conduction pumping lead to flow recirculation near the bottom wall of the minichannel which is expected to deplete the thermal boundary layer, augment mixing and increase the heat transfer. This effect is similar to that produced by solid flow disruptions in the channel wall [42]. However, the geometrical drag induced by solid flow obstacles will lead to higher pressure drop penalty than that produced by flat plate electrodes with negligible thickness. It is to be noted that the EHD generated vortices towards the end of the minichannel can lead to flow reversal, especially at lower Reynolds numbers. Thus, in actual experimental designs sufficient downstream length must be provided between the last electrode and the outlet of the channel.

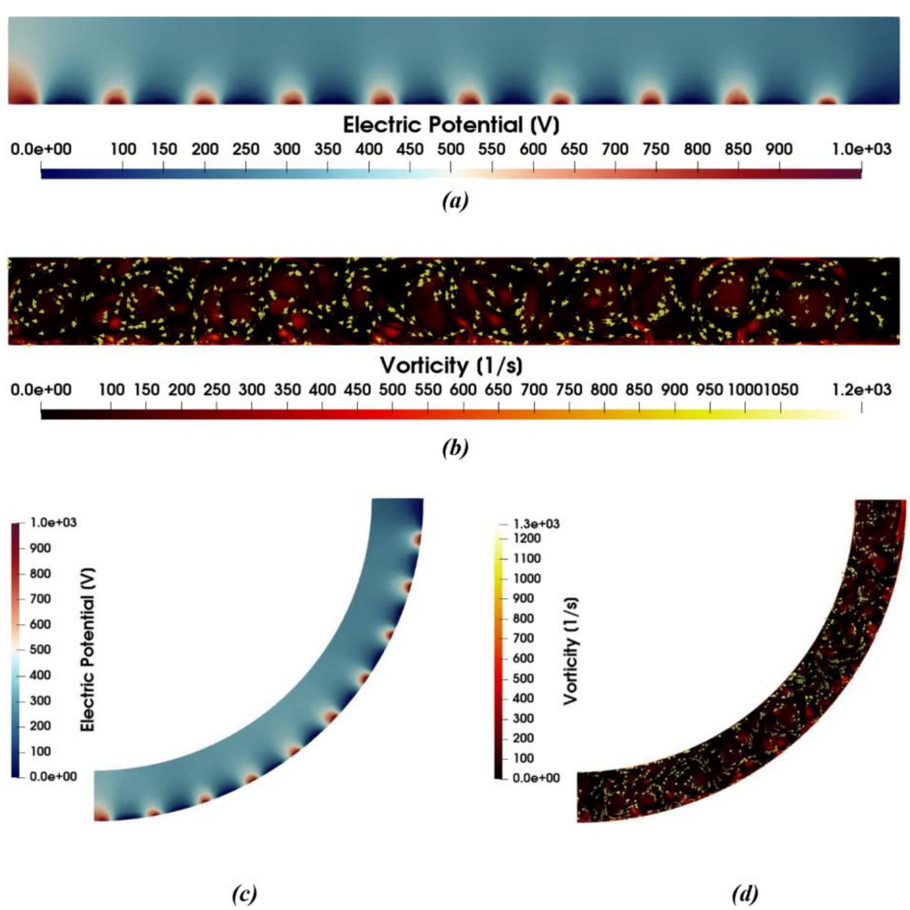

Fig. 4. Contours of electric potential (a and c) and vorticity distribution (b and d) in cases A and B with no external flow and heat flux at an applied voltage of 1 kV.

4.2. Boundary layer depletion by EHD conduction pumping

To visualize the interaction of the EHD vortices with the boundary layers of the inlet flow in the minichannel, the velocity and Q-criterion contours at $Re = 10, 100$ and 1000 and at applied electric potential $V = 0, 0.5$ and 1 kV for both the cases A and B are presented in Figs. 5, 6, 8 and 9. As observed in the velocity and vorticity contours at 0 kV, the flow is evidently laminar and the laminar viscous boundary layer is prominent. It is obvious that the velocity distribution gets higher and the viscous boundary layer gets thinner with increasing values of Reynolds number. The laminar viscous boundary layer observed in the range of Reynolds number considered in this study, restricts fluid mixing and heat transfer from the bottom heated wall. Consequently, thick thermal boundary layers with high temperature distribution are observed in the temperature contours for the cases without any electric field (see Figs. 7 and 10). In Figs. 7 and 10 (cases with $V = 0kV$), a well-defined thermal boundary layer is noted with high temperature distribution. As the flow Reynolds number increases from 10 to 1000, the thermal boundary gets thinner due to increased convection heat transfer. This behavior is common to both the cases of horizontal minichannel (case A) and 90° bent minichannel (case B). In Figs. 5, 6, 8 and 9, the velocity and Q-criterion distribution for the cases with applied electric potential 0.5 and 1 kV are presented. In the presence of EHD conduction pumping, vortices that are perpendicular to the main inlet flow are generated. These vortices disrupt the laminar viscous boundary layer. At $Re = 10$, significant viscous boundary layer disruption and fluid mixing are noted in the computational domain. The vortices generated by EHD conduction pumping phenomenon exhibit sharp increased velocities near the bottom wall. As the Reynolds number of the inlet flow is increased, the inertia of the main channel flow begins to suppress the EHD conduction pumping vortices. Thus, at $Re = 100$, the EHD conduction pumping vortices and the fluid mixing is more localized only near the bottom wall of the channel. However, the viscous boundary layer disruption is still evidently visible at $Re = 100$ and $V = 1kV$. At $Re = 1000$, the EHD conduction pumping vortices are almost completely suppressed by the inertia of the main inlet flow. Thus, boundary layer depletion is not clearly visible in the contours. This flow characteristics is recurrent in both cases A and B of the minichannel. The fluid mixing and rotation induced by the EHD conduction pumping generated vortices are clearly visible in the Q-criterion contours presented in Figs. 6 and 9. Although the viscous boundary layer depletion is not clearly visible in the velocity contours presented in Figs. 5 and 8, at Reynolds number equal to 1000, Q-criterion contour shows the rotating flow near the electrodes even at $Re = 1000$. However, it is evident that the rotational motion and mixing effect introduced by the EHD vortices get weaker with increase in inlet flow Reynolds number. Corresponding to the velocity and vorticity distributions observed in the presence of EHD conduction pumping, the thermal field is visualized in Figs. 7 and 10. As expected, the thermal boundary layer also undergoes disruption and lower temperature is noted in the presence of EHD conduction pumping. In both the cases A and B, the depletion of the thermal boundary layer and mixing of the thermal plumes is clearly evident at $Re = 10$. However, at $Re = 100$, the thermal boundary layer depletion is more notable in case A as compared to case B. This can be attributed to the stronger natural convection in case B. The natural convection due to the bent orientation of the channel adds up to the forced convection of the incoming flow. Thus, the convection effects are stronger and leads to higher suppression of the depletion effect introduced by the EHD conduction pumping vortices. At $Re = 1000$, the thermal boundary layer depletion is almost completely suppressed in both cases A and B. In general, it can be inferred that the boundary layer depletion and mixing effect introduced by the EHD conduction pumping phenomenon is significant at lower Reynolds numbers and higher applied voltages. This statement is applicable for both the horizontal (case A) and 90° bent (case B) configurations of the minichannel.

4.3. Pressure drop

In Fig. 11, the time averaged values of the mean velocity in the flow domain is plotted against the flow Reynolds number for applied electric potential 0, 0.5 and 1kV and at cases A and B. The mean velocity in the domain remains unaffected by the EHD vortices. Although the EHD vortices exhibit sharp velocities, those are localized to the proximity of electrodes and has insignificant influence on the mean velocity in the flow domain dictated by the main inlet flow. Thus, cases with ($V > 0kV$) and without ($V = 0kV$) EHD conduction pumping exhibit same mean

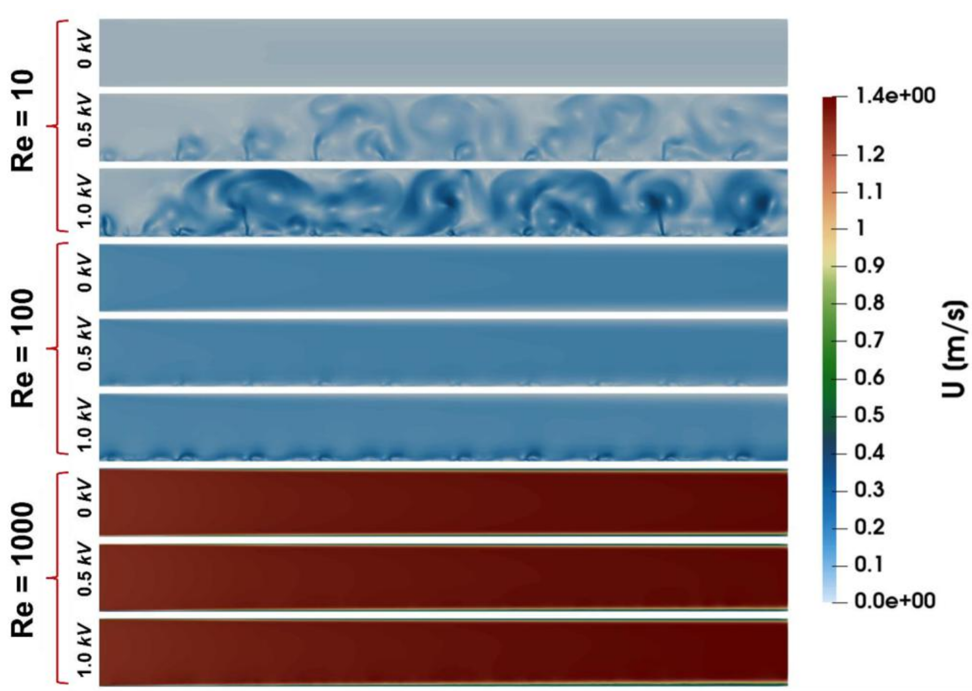

Fig. 5. Velocity field at $Re = 10, 100\,\&\,1000$, applied voltages 0 kV, 0.5 kV and 1 kV and heat flux $q_w = 10000\,W/m^2$ in horizontal configuration (case A).

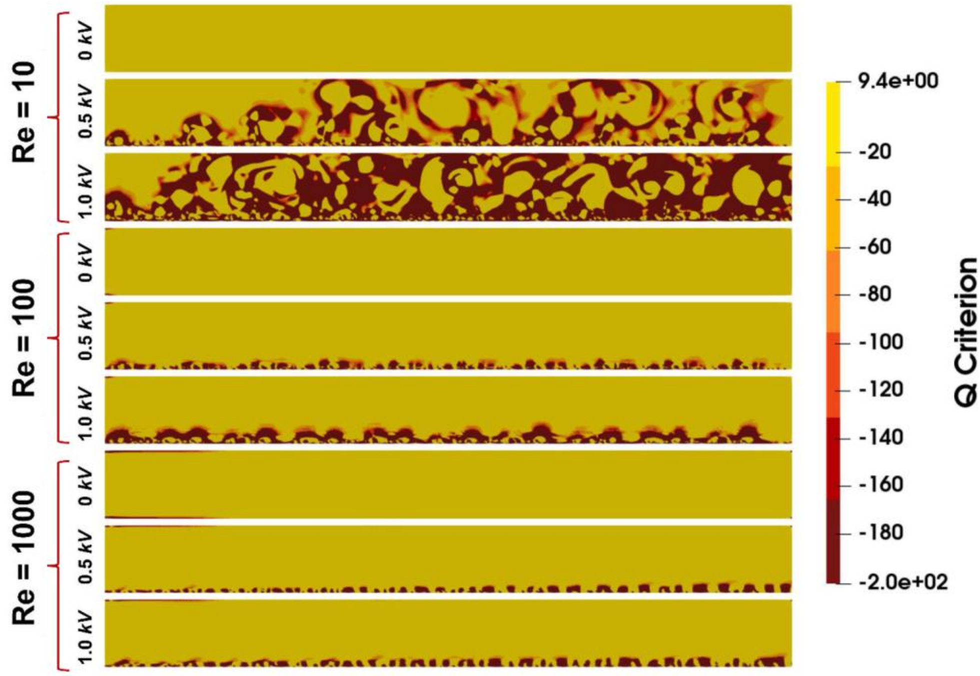

Fig. 6. Vorticity distribution at $\mathbf{Re} = 10, 100\,\&\,1000$, applied voltages 0 kV, 0.5 kV and 1 kV and heat flux $\mathbf{q_w} = 10000\,\mathbf{W/m^2}$ in horizontal configuration (case A).

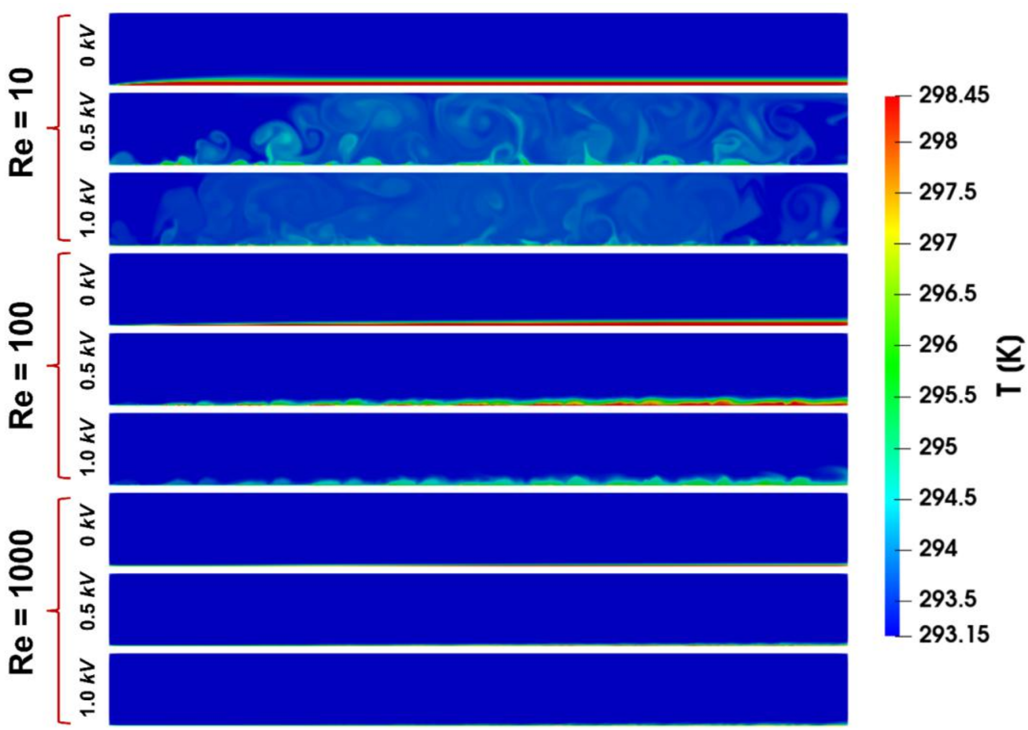

Fig. 7. Temperature field at $\mathbf{Re} = 10, 100\,\&\,1000$, applied voltages 0 kV, 0.5 kV and 1 kV and heat flux $\mathbf{q_w} = 10000\,\mathbf{W/m^2}$ in horizontal configuration (case A).

velocities at all Reynolds numbers. This is true for both the horizontal and 90° degrees bent configuration of the minichannel. In case B, the mean velocity at all Reynolds number is slightly lower than that in case A, due to the additional static pressure in the bent orientation of the minichannel. However, we can infer that the EHD conduction pumping induced vortices are a local phenomenon that is significant only in the region close to the electrodes in the bottom wall. The main stream flow due to the inlet Reynolds number remains unaffected by the introduction of EHD conduction pumping induced vortices. The time averaged pressure drops in cases A and B at $V = 0, 0.5$ and $1\ kV$ is plotted as a function of flow Reynolds number in Fig. 12. It is obvious that the pressure drop increases with increase in Reynolds number for both the cases A and B. The pressure drops are higher for case B due to the additional static pressure in the bent orientation of the minichannel. As observed in the contours of velocity and q-criterion presented in Figs. 6 and 9, the EHD generated vortices are perpendicular to the incoming

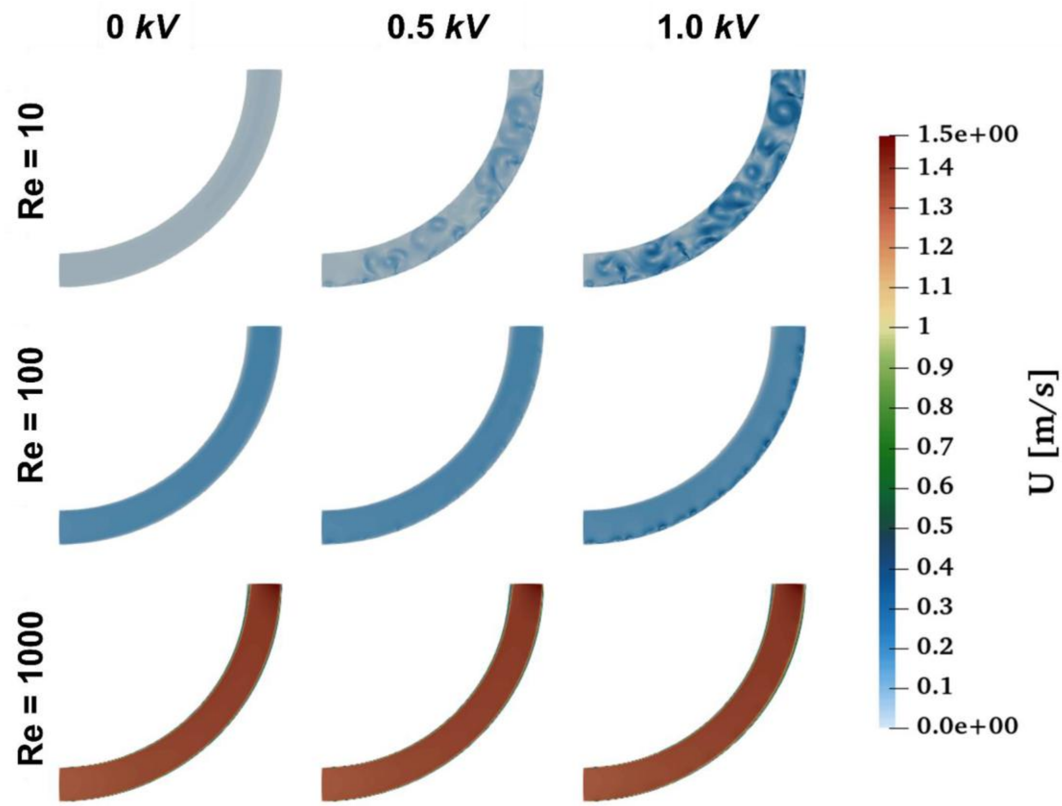

Fig. 8. Velocity field at **Re** $= 10, 100 \& 1000$, applied voltages 0 kV, 0.5 kV and 1 kV and heat flux $\mathbf{q_w} = 10000\,\mathbf{W/m^2}$ in bent configuration (case B).

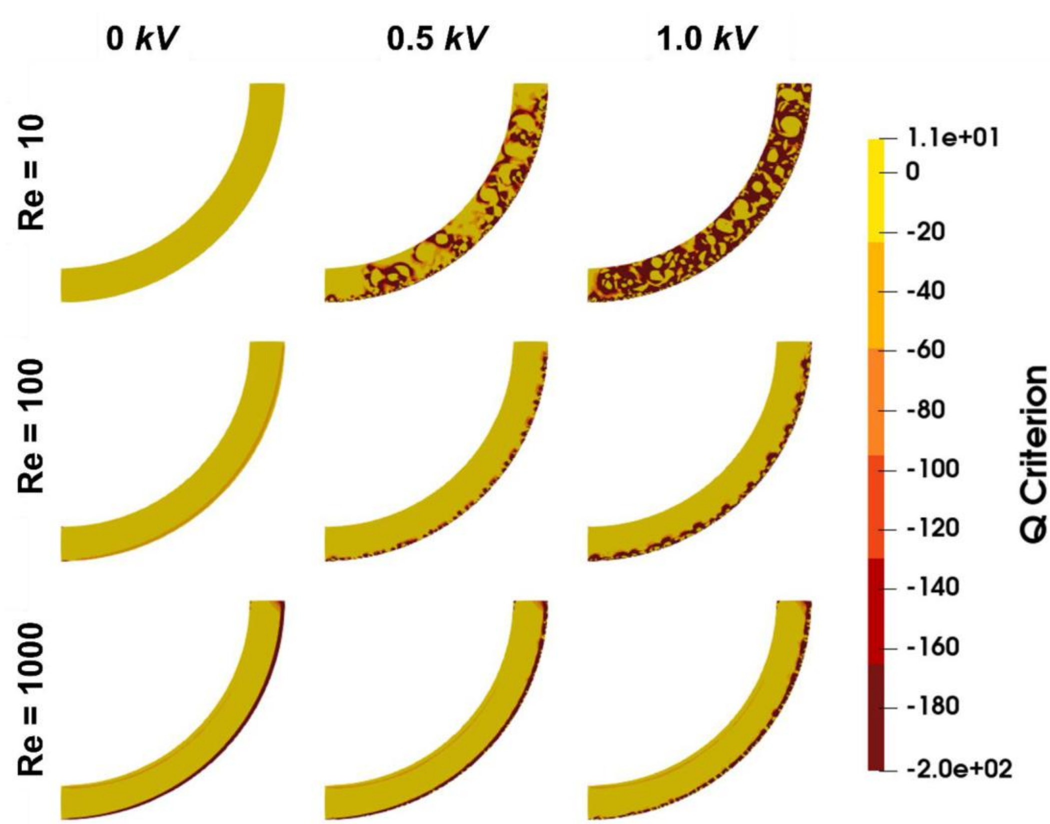

Fig. 9. Vorticity distribution at **Re** $= 10, 100 \& 1000$, applied voltages 0 kV, 0.5 kV and 1 kV and heat flux $\mathbf{q_w} = 10000\,\mathbf{W/m^2}$ in bent configuration (case B).

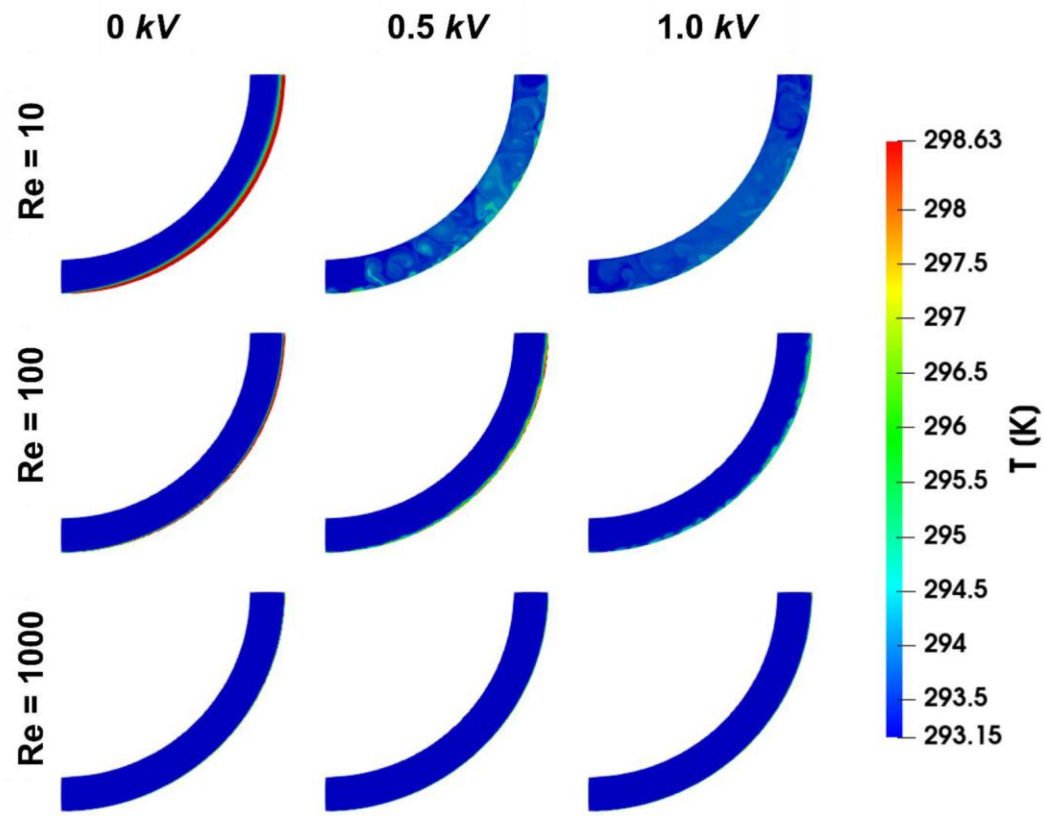

Fig. 10. Temperature field at **Re** $= 10, 100\,\&\,1000$, applied voltages 0 kV, 0.5 kV and 1 kV and heat flux $\mathbf{q_w} = 10000\,\mathbf{W/m^2}$ in bent configuration (case B).

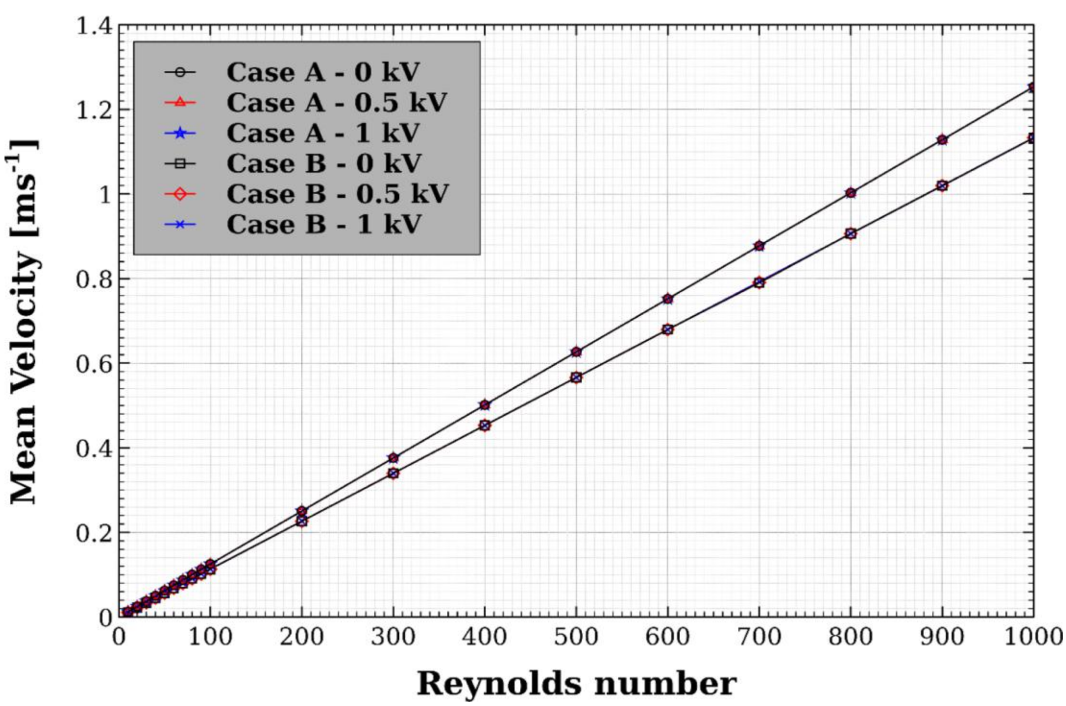

Fig. 11. Variation of mean velocity at $10 \leq \mathbf{Re} \leq 1000$ and applied voltages 0 kV, 0.5 kV & 1 kV for cases A and B.

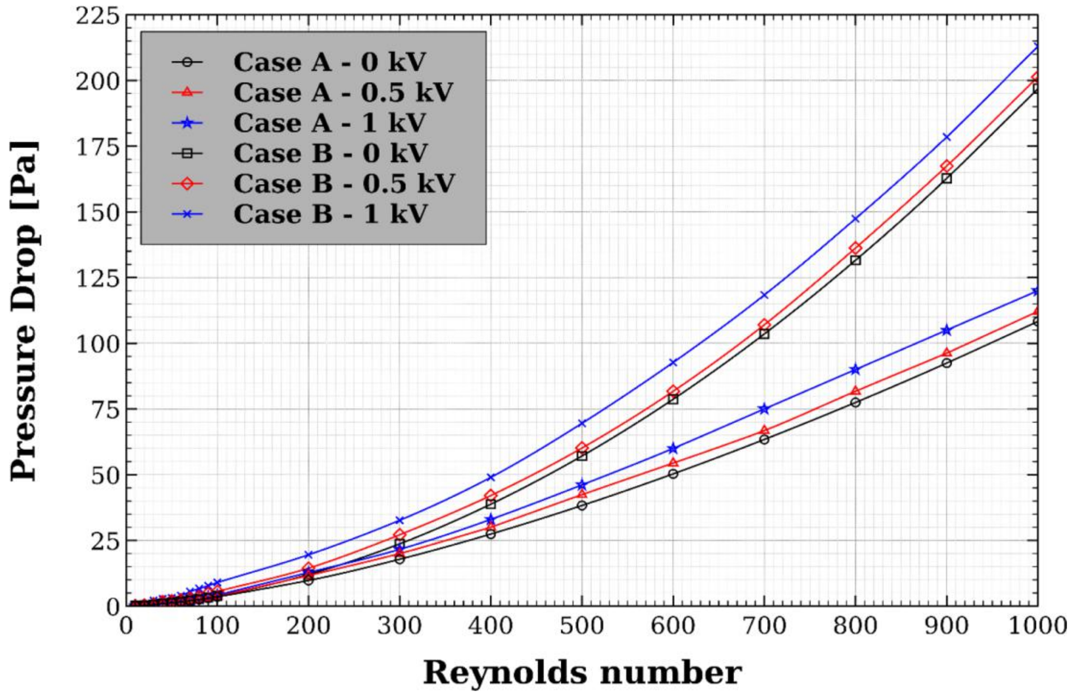

Fig. 12. Variation of pressure drop at $10 \leq \mathbf{Re} \leq 1000$ and applied voltages 0 kV, 0.5 kV & 1 kV for cases A and B.

flow. These vortices induce a drag to the mainstream fluid flow leading to additional pressure drop. Thus, it is noted that the pressure drop increases with the increase in applied voltage. At any given value of Re, the time averaged pressure drop value between the inlet and out of the minichannel increases with the increase in applied voltage.

4.4. Heat transfer

The flow morphology, depletion of thermal boundary layer, mixing and increase in heat transfer is already demonstrated qualitatively in the velocity, Q-criterion and temperature contours presented in Figs. 5 – 10. The increase in heat transfer due to the thermal boundary layer depletion is quantified in terms of mean and local Nusselt number in Figs. 13 and 14. It is to be noted that the main inlet flow decided by the Reynolds number considered in the study is in the laminar steady regime. The unsteadiness introduced by the EHD vortices is very small and is notable only at smaller values of Reynolds numbers ($Re < 100$). Even at $Re < 100$, the amplitude of oscillation in the local values with respect to time is very small. Thus, the local Nusselt number values presented in Fig. 13 are at time $t = 10s$. It is verified that all the simulations reach a statistically steady state well before 10 s. Local Nusselt number distribution along the heated bottom wall for cases A & B at $Re = 10$, 100 & 1000 and $V = 0$ & 1 kV are presented in Fig. 13 (a – b). In the absence of EHD conduction pumping, the local Nusselt profile along the bottom heated wall exhibits a smooth profile. For case A, the local Nusselt number is highest at the inlet, gradually falls in the entry region and reaches a constant value towards the outlet of the minichannel. For case B, the local Nusselt number is maximum at the inlet, undergoes a gradual decrease in the flow developing region. Unlike case A, the local Nusselt number distribution exhibits a gradual raise towards the outlet of the minichannel, due to the stronger natural convection in the bent configuration of case B. In the absence of EHD conduction pumping, the increase in local Nusselt number distribution due to the increase in Reynolds number is evident in both cases A and B. The local Nusselt number distribution in the presence of EHD conduction pumping is characterized by ups and downs along the length of the bottom heated wall. This can be attributed to the increased heat transfer and thermal boundary layer disruption caused by the EHD conduction pumping vortices. The local Nusselt number distribution in the presence of EHD conduction pumping is notably higher than at $0kV$, for both cases A & B. The increase is higher for $Re = 10$. In fact, the local Nusselt number distribution is more or less same for $Re = 100$ and 1000 at an applied voltage of 1 kV. This indicates that at $Re = 10$, the local Nusselt number distribution along the heated wall is mainly governed by the thermal boundary layer depletion caused by the EHD conduction pumping vortices. As the flow Reynolds number increases, the inertia of the main inlet flow begins to suppress the EHD conduction pumping induced vortices and the resultant heat transfer enhancement. The mean Nusselt number variation with respect to Reynolds number at 0, 0.5 and 1 kV for cases A & B is presented in Fig. 14. The mean Nusselt number presented in Fig. 14 are averaged values for a period of 10 s. In general, the mean Nusselt number is more or less same for cases A and B. In the absence of EHD conduction pumping, for both cases A & B, the mean Nusselt number gradually increases with the increase in Reynolds number. At higher Reynolds numbers, the mean Nusselt number for case B is slightly higher than case A due to the stronger flow observed near the outlet of the minichannel. For both cases A and B, the mean Nusselt numbers in the presence of EHD conduction pumping are notably higher than at $0kV$, for all Reynolds numbers. At $V = 0.5$ and 1 kV, for both cases A and B, the mean Nusselt number is more or less same. This confirms that the heat transfer from the wall is mainly dictated by the local thermal boundary layer depletion brought about by the EHD conduction induced vortices. Although the thermal boundary layer depletion is not distinctly visible at $Re = 1000$ (see Figs. 7 and 10), the EHD conduction vortices still influences the heat transfer. Thus, it can be inferred that the local heat transfer enhancement due to the EHD conduction pumping vortices is functional irrespective of the flow Reynolds number and channel orientation in the parameter space of this study. The maximum Nusselt number is noted at $Re = 10$ for both cases A and B. Then, the mean Nusselt number falls abruptly followed by a gradual increase and gets saturated at higher Reynolds numbers. The heat transfer enhancement is very significant at lower Reynolds numbers and higher applied electric potentials, for both cases A and B.

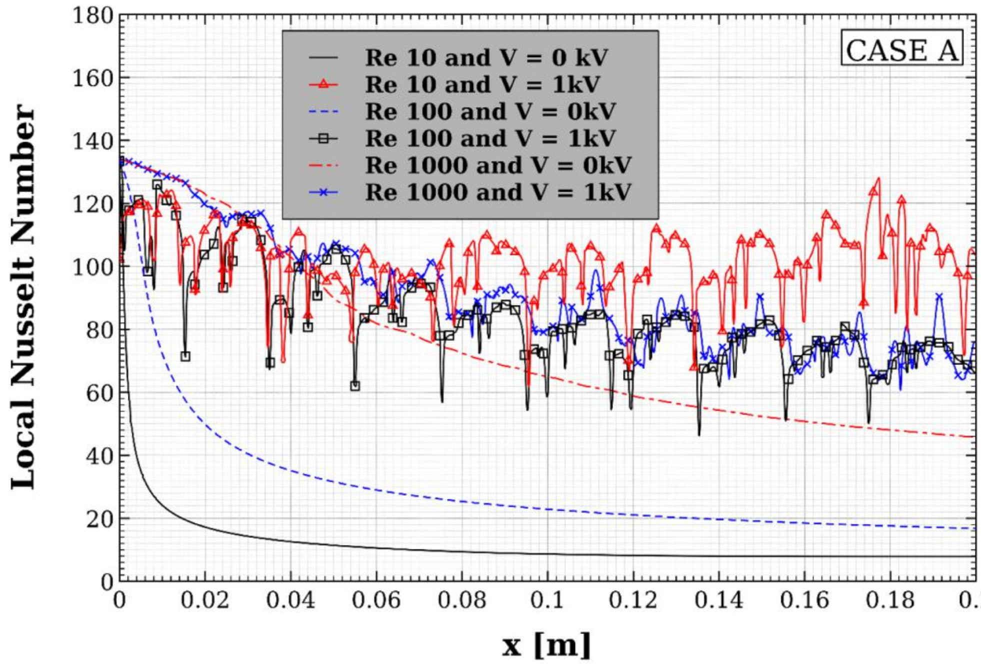

(a)

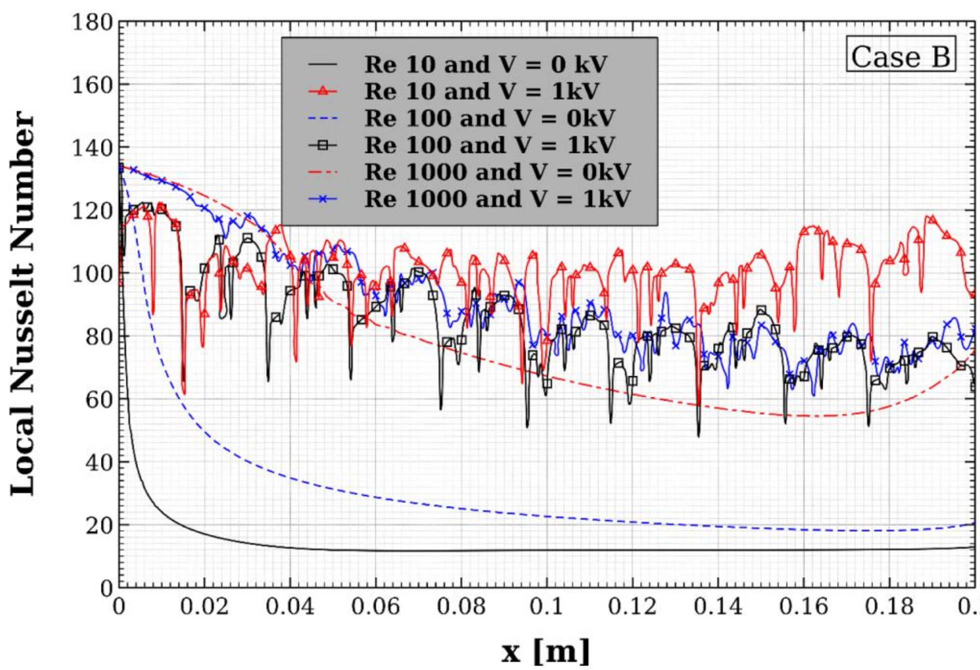

(b)

Fig. 13. Local Nusselt number distribution along the bottom heated wall at $10 \leq \mathbf{Re} \leq 1000$ and applied voltages 0 kV, 0.5 kV & 1 kV for cases A (a) and B (b).

4.5. Performance evaluation

The enhancement in heat transfer caused by the EHD conduction pumping is also accompanied by a corresponding increase in pressure drop. However, it is to be noted that the pressure drop is minimal as compared to the increase in mean and local Nusselt numbers (refer Figs. 12 - 14). The performance factor *PF*, which is defined as a combined function of heat transfer enhancement and pressure drop, is used to evaluate the net performance of the minichannel [36]. When the *PF* is greater than 1, the heat transfer enhancement due to the EHD conduction pumping is higher than the incurred penalty in pressure drop. By contrast, when $PF < 1$, the pressure drop penalty is higher than the achieved increase in heat transfer. For both cases A & B, the *PF* is higher at lower Reynolds numbers and gets lower as Re is increased. A maximum *PF* around 8.5 is observed for $Re = 10$ and $V = 1kV$ for case A. Whereas for case B, the maximum *PF* at for $Re = 10$ and $V = 1kV$ is around 6.9. The effect of curvature on performance factor is notable only at lower Reynolds numbers and at higher applied voltages. Irrespective

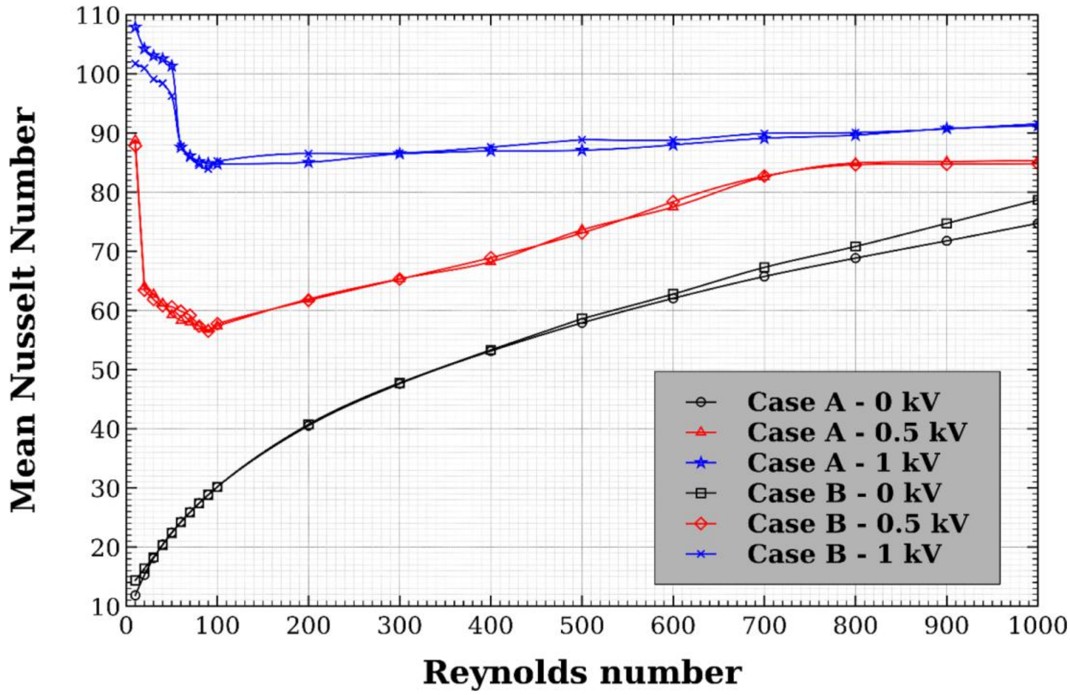

Fig. 14. Variation of mean Nusselt number at $10 \leq \mathbf{Re} \leq 1000$ and applied voltages 0 kV, 0.5 kV & 1 kV for cases A and B.

of the curvature, at any given applied voltage, the performance factor is more or less same for Reynolds number greater than 400. At $Re > 400$, the performance factor for all cases is only slightly above 1, in both cases and applied voltages. This confirms that the EHD vortices have weak influence in performance factor enhancement at higher voltages. At lower Reynolds numbers, the effect of curvature and applied voltage is evidently visible. As presented in Fig. 12, we notice that the pressure drop incurred in case B (bent configuration) is higher than that observed in case B. Whereas, the mean Nusselt number presented in Fig. 14 is more or less same for horizontal and bent configuration. Thus, for a same increase in heat transfer, case B leads to additional pressure drop. This can be related with the lower mean velocity in case B (refer Fig. 11). Thus, the performance factor in case A is slightly higher than that in case B. In conclusion, it can be inferred that EHD vortices significantly increase the performance factor at lower Reynolds numbers. The increase in mean Nusselt number caused by the EHD vortices is same irrespective of the curvature of the minichannel. However, the additional pressure drop caused by EHD vortices is higher in curved configuration (Case B). This leads to slightly higher performance factor in case A, as compared to case B. However, for both the cases A & B and in the entire parameter

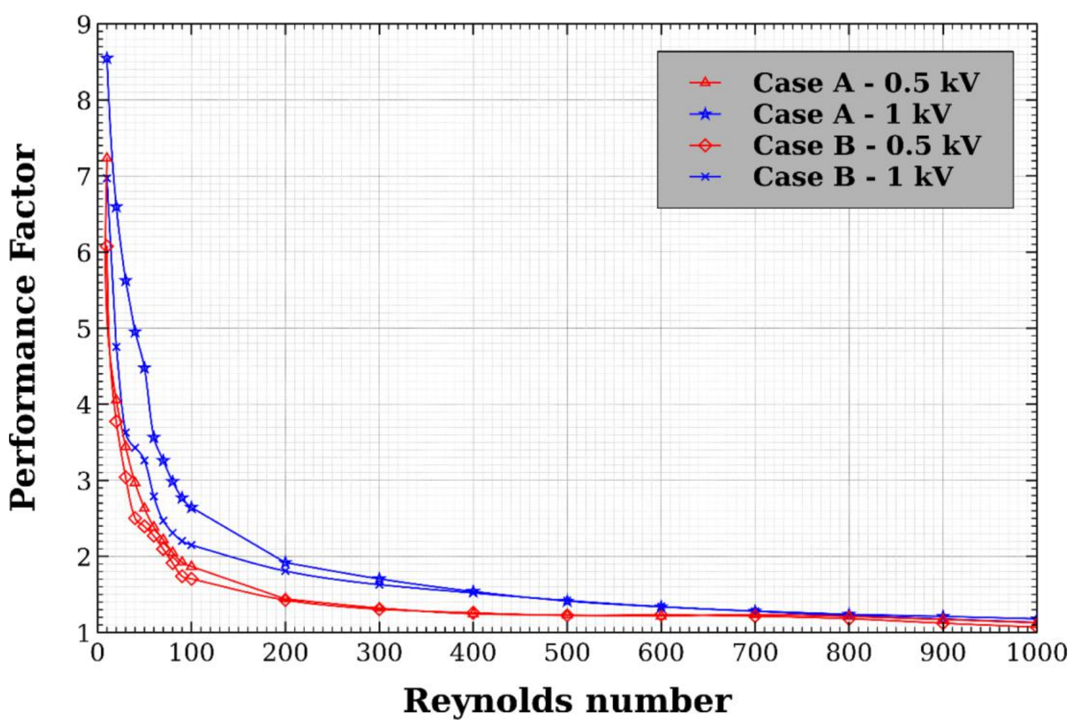

Fig. 15. Variation of performance factor at $10 \leq \mathbf{Re} \leq 1000$ and applied voltages 0.5 kV & 1 kV for cases A and B.

space considered herein, the performance factor is greater than 1 (refer Fig. 15). This indicates that EHD conduction pumping brings an effective increase in heat transfer with comparably smaller increase in pressure drop.

The electric power consumed by EHD conduction pumping is calculated as $P_{EL} = V \times I_{tot}$, where I denotes the electric current flowing from the high-voltage electrodes to the grounded electrodes. The total electric current is computed by integrating the net current density flux $\overrightarrow{J}$ over the surface of all the high-voltage electrodes as follows [41]:

$$I_{tot} = \iint \overrightarrow{J}.\widehat{n}dS \tag{13}$$

where,

$$\overrightarrow{J} = \frac{\partial \varepsilon_f \overrightarrow{E}}{\partial t} + (Kp + Kn)\overrightarrow{E} + (p - n)\overrightarrow{u} - (D\nabla p - D\nabla n) \tag{14}$$

The time averaged electric power consumption is 16.112 mW at $Re = 1000$ and V = 1kV for case A and 23.5643 mW at $Re = 1000$ and V = 1kV for case B. Thus, EHD conduction pumping results in notable increase in heat transfer and performance factor at the expense of few milliwatts of additional electric power consumption. Thus, thermal boundary layer depletion by vortices generated by EHD conduction pumping due to thin plate electrodes flushed to the channel walls is an effective active method of heat transfer enhancement in a minichannel.

5. Concluding remarks

In this work, a 2D numerical investigation of the flow and heat transfer in straight and curved minichannels are presented. The flow and heat transfer performance at straight horizontal (case A) and 90° bent (case B) configurations are evaluated. The mechanism of boundary layer disruption and the resultant enhancement in heat transfer at different flow Reynolds numbers Re and applied electric potentials are investigated. The main conclusions of this study based on an analysis of the results are as follows:

- The electrode pairs flushed on to the bottom of the minichannel generates small vortices due to EHD conduction pumping. These EHD vortices exhibit localized high velocities close to the bottom wall.
- The viscous and thermal boundary layers are effectively disrupted by the EHD-induced vortices, leading to notable increase in mean and local Nusselt numbers.
- For the parameters considered in this study, the performance factor in the presence of EHD conduction pumping is always greater than 1, for both cases A and B. This indicates that the heat transfer enhancement obtained by generating EHD vortices is higher than the incurred additional pressure drops.
- Maximum performance factors around 8.5 and 7 are achieved in straight and curved orientations of the channel, respectively. Maximum performance enhancement is observed at low Reynolds numbers and high applied voltages.
- The performance in 90° bent orientation (case B) is lower than that in case A (horizontal orientation). A maximum of 18.5 % drop in performance is noted in case B, as compared to case A.
- The additional electric power consumption for the EHD conduction pumping is only in the range of few milliwatts. This proves that the EHD conduction based thermal boundary layer depletion is an effective active technique for active enhancement in minichannels.

In this study, a novel method is proposed to disrupt the laminar viscous and thermal boundary layers in a flexible minichannel by using the vortices generated by EHD conduction pumping phenomenon. The results indicate that at safe and low applied voltages with minimum additional power consumption, EHD conduction pumping can potentially be used to enhance the heat transfer in a flexible minichannel.

Declaration of Competing Interest

The authors declare that they have no known competing financial interests or personal relationships that could have appeared to influence the work reported in this paper.

Data availability

Data will be made available on request.

Acknowledgments

This work was supported by National Research Foundation of Korea (NRF) grant funded by the Korea government (MSIT) (No. 2021R1C1C1012119), and the Industrial Technology Innovation Program (No. 20007058, Development of safe and comfortable human augmentation hybrid robot suit) funded by the Ministry of Trade, Industry & Energy (MOTIE, Korea).

References

[1] Z. Zhang, X. Wang, Y. Yan, A review of the state-of-the-art in electronic cooling, E-Prime-Adv. Electrical Eng. Electronics and Energy. 1 (2021), 100009.
[2] S.G. Kandlikar, History, advances, and challenges in liquid flow and flow boiling heat transfer in microchannels: a critical review, J. Heat Transfer. 134 (2012).
[3] N.A.C. Sidik, M.N.A.W. Muhamad, W.M.A.A. Japar, Z.A. Rasid, An overview of passive techniques for heat transfer augmentation in microchannel heat sink, Int. Commun. Heat Mass Transfer 88 (2017) 74–83.
[4] C.-Y. Lee, W.-T. Wang, C.-C. Liu, L.-M. Fu, Passive mixers in microfluidic systems: a review, Chem. Eng. J. 288 (2016) 146–160.
[5] A. Banerjee, A.K. Nayak, B. Weigand, Enhanced mixing and flow reversal in a modulated microchannel, Int. J. Mech. Sci. 155 (2019) 430–439.
[6] T. Dixit, I. Ghosh, Review of micro- and mini-channel heat sinks and heat exchangers for single phase fluids, Renew. Sustain. Energy Rev. 41 (2015) 1298–1311, https://doi.org/10.1016/j.rser.2014.09.024.
[7] A.A. Hussien, M.Z. Abdullah, M.A. Al-Nimr, Single-phase heat transfer enhancement in micro/minichannels using nanofluids: theory and applications, Appl. Energy. 164 (2016) 733–755, https://doi.org/10.1016/j.apenergy.2015.11.099.
[8] C. Wang, Q. Lu, Y. Liu, H. Huang, J. Sun, Progressive review of heat transfer enhancement technologies in 2010–2020, Sustainable Energy Technol. Assess. 56 (2023), 103121, https://doi.org/10.1016/j.seta.2023.103121.
[9] J. Seyed-Yagoobi, Electrohydrodynamic pumping of dielectric liquids, J. Electrostat. 63 (2005) 861–869.
[10] J.M. Crowley, P. Chang, D. Riley, J.C. Chato, EHD induction pumping in annuli, IEEE Trans. Electr. Insul. 413–418 (1985).
[11] A. Castellanos, Electrohydrodynamics, Springer Science & Business Media, 1998.
[12] S.-I. Jeong, J. Seyed-Yagoobi, Experimental study of electrohydrodynamic pumping through conduction phenomenon, J. Electrostat. 56 (2002) 123–133.
[13] P.A. Vázquez, M. Talmor, J. Seyed-Yagoobi, P. Traoré, M. Yazdani, In-depth description of electrohydrodynamic conduction pumping of dielectric liquids: physical model and regime analysis, Phys. Fluids 31 (2019), 113601.
[14] P. Atten, J. Seyed-Yagoobi, Electrohydrodynamically induced dielectric liquid flow through pure conduction in point/plane geometry, IEEE Trans. Dielectr. Electr. Insul. 10 (2003) 27–36.
[15] S.-I. Jeong, J. Seyed-Yagoobi, P. Atten, Theoretical/numerical study of electrohydrodynamic pumping through conduction phenomenon, IEEE Trans. Ind. Appl. 39 (2003) 355–361.
[16] S.I. Jeong, J. Seyed-Yagoobi, Fluid circulation in an enclosure generated by electrohydrodynamic conduction phenomenon, IEEE Trans. Dielectr. Electr. Insul. 11 (2004) 899–910.
[17] Y. Feng, J. Seyed-Yagoobi, Understanding of electrohydrodynamic conduction pumping phenomenon, Phys. Fluids 16 (2004) 2432–2441.
[18] Y. Feng, J. Seyed-Yagoobi, Electrical charge transport and energy conversion with fluid flow during electrohydrodynamic conduction pumping, Phys. Fluids 19 (2007) 57102.
[19] M.R. Pearson, J. Seyed-Yagoobi, Advances in electrohydrodynamic conduction pumping, IEEE Trans. Dielectr. Electr. Insul. 16 (2009) 424–434.
[20] M.A.W. Siddiqui, J. Seyed-Yagoobi, Experimental study of pumping of liquid film with electric conduction phenomenon, IEEE Trans. Ind. Appl. 45 (2009) 3–9.
[21] M.R. Pearson, J. Seyed-Yagoobi, Experimental study of EHD conduction pumping at the meso-and micro-scale, J. Electrostat. 69 (2011) 479–485.
[22] I. Kano, T. Nishina, Effect of electrode arrangements on EHD conduction pumping, IEEE Trans. Ind. Appl. 49 (2013) 679–684.

[23] V.K. Patel, J. Seyed-Yagoobi, Long-term performance evaluation of microscale two-phase heat transport device driven by EHD conduction, IEEE Trans. Ind. Appl. 50 (2014) 3011–3016.
[24] Z. Du, J. Huang, Q. Liu, R. Deepak Selvakumar, J. Wu, Numerical investigation on electrohydrodynamic conduction pumping with an external flow, Phys. Fluids 33 (2021), 123609.
[25] M.R. Pearson, J. Seyed-Yagoobi, Electrohydrodynamic conduction driven single- and two-phase flow in microchannels with heat transfer, J. Heat Transfer. 135 (2013).
[26] M.R. Pearson, J. Seyed-Yagoobi, Single-and two-phase flow in microchannels with heat transfer and driven by an EHD conduction pump, in, ASME Int. Mechan. Eng. Congress and Exposition (2011) 937–952.
[27] M.R. Pearson, J. Seyed-Yagoobi, Experimental study of linear and radial two-phase heat transport devices driven by electrohydrodynamic conduction pumping, J. Heat Transfer. 137 (2015).
[28] V.K. Patel, J. Seyed-Yagoobi, S. Sinha-Ray, S. Sinha-Ray, A. Yarin, Electrohydrodynamic conduction pumping-driven liquid film flow boiling on bare and nanofiber-enhanced surfaces, J. Heat Transfer. 138 (2016).
[29] R.D. Selvakumar, D. Zhonglin, J. Wu, Heat transfer intensification by EHD conduction pumping for electronic cooling applications, Int. J. Heat Fluid Flow. 95 (2022), 108972.
[30] M. Mirzaei, M. Saffar-Avval, Enhancement of convection heat transfer using EHD conduction method, Exp. Therm. Fluid Sci. 93 (2018) 108–118.
[31] L. Onsager, Deviations from Ohm's law in weak electrolytes, J Chem Phys. 2 (1934) 599–615.
[32] Y.K. Suh, Modeling and simulation of ion transport in dielectric liquids-Fundamentals and review, IEEE Trans. Dielectr. Electr. Insul. 19 (2012) 831–848.
[33] A. Castellanos, Coulomb-driven convection in electrohydrodynamics, IEEE Trans. Electr. Insul. 26 (1991) 1201–1215, https://doi.org/10.1109/14.108160.
[34] J. Wu, P. Traoré, A finite-volume method for electro-thermoconvective phenomena in a plane layer of dielectric liquid, Numeri Heat Transf. A Appl. 68 (2015) 471–500.
[35] G. Xia, L. Chai, H. Wang, M. Zhou, Z. Cui, Optimum thermal design of microchannel heat sink with triangular reentrant cavities, Appl. Therm. Eng. 31 (2011) 1208–1219.
[36] H. Lu, M. Xu, L. Gong, X. Duan, J.C. Chai, Effects of surface roughness in microchannel with passive heat transfer enhancement structures, Int. J. Heat Mass Transf. 148 (2020), 119070.
[37] B. van Leer, Towards the ultimate conservative difference scheme, J. Comput. Phys. 135 (1997) 229–248.
[38] F. Moukalled, L. Mangani, M. Darwish, others, The finite volume method in computational fluid dynamics, An Advanced Introduction with OpenFoam® and Matlab®. Nueva York: Springer. Recuperado de Http://Www. Gidropraktikum. Narod. Ru/Moukalled-et-al-FVM-OpenFOAM-Matlab. Pdf. (2016).
[39] T.L. Bergman, A.S. Lavine, F.P. Incropera, D.P. DeWitt, Introduction to heat transfer, John Wiley & Sons, 2011.
[40] D. v Fernandes, D.S. Cho, Y.K. Suh, Electrohydrodynamic flow of dielectric liquid around a wire electrode-effect of truncation of Onsager function, IEEE Transactions on Dielectrics and Electrical Insulation. 21 (2014) 194–200.
[41] U.K. Seth, Message Passing Interface parallelization of a multi-block structured numerical solver, Application to the numerical simulation of various typical Electro-Hydro-Dynamic flows, Poitiers, 2019.
[42] M. Kadivar, D. Tormey, G. McGranaghan, CFD of roughness effects on laminar heat transfer applied to additive manufactured minichannels, Heat Mass Transf. (2022), https://doi.org/10.1007/s00231-022-03268-1.